

## Seismic reflection imaging of shallow oceanographic structures

Helen Piété,<sup>1</sup> Louis Marié,<sup>2</sup> Bruno Marsset,<sup>3</sup> Yannick Thomas,<sup>3</sup>  
and Marc-André Gutscher<sup>1</sup>

Received 4 September 2012; revised 5 March 2013; accepted 6 March 2013; published 8 May 2013.

[1] Multichannel seismic (MCS) reflection profiling can provide high lateral resolution images of deep ocean thermohaline fine structure. However, the shallowest layers of the water column ( $z < 150$  m) have remained unexplored by this technique until recently. In order to explore the feasibility of shallow seismic oceanography (SO), we reprocessed and analyzed four multichannel seismic reflection sections featuring reflectors at depths between 10 and 150 m. The influence of the acquisition parameters was quantified. Seismic data processing dedicated to SO was also investigated. Conventional seismic acquisition systems were found to be ill-suited to the imaging of shallow oceanographic structures, because of a high antenna filter effect induced by large offsets and seismic trace lengths, and sources that typically cannot provide both a high level of emission and fine vertical resolution. We considered a test case, the imagery of the seasonal thermocline on the western Brittany continental shelf. New oceanographic data acquired in this area allowed simulation of the seismic acquisition. Sea trials of a specifically designed system were performed during the ASPEX survey, conducted in early summer 2012. The seismic device featured: (i) four seismic streamers, each consisting of six traces of 1.80 m; (ii) a 1000 J SIG sparker source, providing a 400 Hz signal with a level of emission of 205 dB re 1  $\mu$ Pa @ 1 m. This survey captured the 15 m thick, 30 m deep seasonal thermocline in unprecedented detail, showing images of vertical displacements most probably induced by internal waves.

**Citation:** Piété, H., L. Marié, B. Marsset, Y. Thomas, and M.-A. Gutscher (2013), Seismic reflection imaging of shallow oceanographic structures, *J. Geophys. Res. Oceans*, 118, 2329–2344, doi: 10.1002/jgrc.20156.

### 1. Introduction

[2] Ocean waters commonly feature a thermally homogeneous surface layer, whose thickness can reach tens to hundreds of meters depending on the location and the season [De Boyer Montégut *et al.*, 2004]. Klein and Lapeyre [2009] demonstrated that the fine scale physical variations ( $< 500$  m) of the ocean surface layers are able to induce forcings on mesoscale and ocean basin scale structures. However, conventional physical oceanography observation methods cannot image these fine variations. While satellite imagery captures large-scale structures over wide areas, but is restricted to surface observations, lowered or moored expendable Bathymograph (XBT) and CTD probes image fine scale vertical patterns, but only at discrete locations. Towed instruments provide more continuous measurements; nevertheless, the interval between descending and ascending profiles is on

the order of several hundred meters. Otherwise, while high frequency sonars are capable of mapping upper-ocean thermoclines with a higher horizontal resolution [Pingree and Mardell, 1985; Trevorrow, 1998; Klymak and Moum, 2003], they provide images based on acoustic backscattering from suspended sediments, plankton, or turbulence. Thus, the hydrological structure cannot be physically quantified. Accordingly, new methods must be developed in order to observe the fine scale structure of the ocean surface layer.

[3] Multichannel seismics (MCS) may help to image fine scale shallow oceanographic structures. Geologists and the oil industry have used this geophysical technique for over a century in order to study the solid Earth [Sheriff and Geldart, 1982]. Its successful application to the high-resolution observation of the ocean water column has been recently demonstrated [Holbrook *et al.*, 2003; Nandi *et al.*, 2004; Holbrook and Fer, 2005]. Indeed, this technique called seismic oceanography (SO) has yielded images of thermohaline structure at horizontal scales as small as several meters. This represents an improvement of two orders of magnitude compared to conventional oceanographic methods. During the last several years, SO has been extensively used for the studies of the following: (i) fine scale structures associated with thermohaline intrusions [Holbrook *et al.*, 2003], thermohaline staircases [Biescas *et al.*, 2010; Fer *et al.*, 2010] and internal gravity waves [Holbrook and Fer, 2005; Krahmman *et al.*, 2008; Holbrook *et al.*, 2009; Blacic and Holbrook, 2010]; (ii) mesoscale structures such

<sup>1</sup>Laboratoire Domaines Océaniques, IUEM, University of Brest, 29280, Plouzané, France.

<sup>2</sup>Laboratoire de Physique des Océans, IFREMER, Centre de Brest, 29280, Plouzané, France.

<sup>3</sup>Géosciences Marines, IFREMER, Centre de Brest, 29280, Plouzané, France.

Corresponding author: H. Piété, Laboratoire Domaines Océaniques, IUEM, University of Brest, 29280 Plouzané, France. (helen.piete@univ-brest.fr)

as current flows [Tsuji *et al.*, 2005; Nakamura *et al.*, 2006; Mirshak *et al.*, 2010], and eddies and meddies [Biescas *et al.*, 2008; Quentel *et al.*, 2010; Ménesguen *et al.*, 2012].

[4] SO surveys rely on the detection of artificially generated acoustic signals, reflected from oceanographic structure-related physical boundaries within the seawater. The MCS device includes two main components towed behind the vessel:

[5] 1. An impulsive source located below the surface, emitting acoustic waves at periodic time intervals as the ship moves along the transect. Conventional frequencies are on the order of 30–60 Hz for hydrocarbon exploration surveys, 100–300 Hz for high-resolution acquisitions, and 400 to more than 1 kHz for very high-resolution surveys. The lateral resolution of processed images may reach the wavelength of the seismic signal, and thus ranges from 150 to 1.5 m.

[6] 2. A multichannel receiver—seismic streamer—constituted of several groups of hydrophones.

[7] MCS provides an image of the acoustic reflectivity of water masses, which is directly a function of the hydrologic structure. The associated reflection coefficient  $R$  can be defined using the Zoeppritz equations [Zoeppritz, 1919]. Since seawater is an acoustic medium, i.e., it does not permit the propagation of shear waves, these equations can be simplified. Considering the case of a compression wave impacting at an incidence angle  $\theta$ , a reflective interface between two homogeneous layers  $i$  and  $i + 1$ ,  $R$  is expressed in decibels by

$$R = 20 \times \log_{10} \left( \frac{Z_{i+1} \cos\theta_i - Z_i \cos\theta_{i+1}}{Z_{i+1} \cos\theta_i + Z_i \cos\theta_{i+1}} \right) \quad (1)$$

$$\text{with } Z = \rho \times c \quad (2)$$

where  $Z$  is the acoustic impedance,  $\rho$  the density and  $c$  the speed of sound in seawater. The last two parameters are related to temperature and salinity by the equation of state of seawater [Millero *et al.*, 1980]. Temperature contributes predominantly to the seawater sound speed and density variations [Pickard and Emery, 1990; Sallarès *et al.*, 2009]. Other workers demonstrated that seismic sections can therefore, as a first approximation, be considered as actual maps of vertical temperature gradients [Ruddick *et al.*, 2009]. Combined with simultaneous XBT measurements, MCS provides a detailed picture of the water column structure. Temperature contrasts as small as 0.03°C can be detected by an appropriate MCS device [Nandi *et al.*, 2004].

[8] Nevertheless, until now, SO studies have focused on structures deeper than 150 m. The shallowest levels of the water column have remained unexplored by seismic reflection methods. However, the pioneering works of Phillips and Dean [1991] and Géli *et al.* [2005], followed by the recent study of Carniel *et al.* [2012] have demonstrated that MCS is potentially a well-suited technique for imaging the upper-ocean structure.

[9] We take this technique one step further by examining existing data sets acquired in the North Atlantic Ocean and Mediterranean Sea that feature reflections from shallow (10–150 m) oceanographic structures. We then verify our findings by devising an optimal seismic setup that is suited

to the imaging of the upper layers of the ocean and test it against the results from the existing data sets. As we will show, it is possible with this acquisition scheme to provide high lateral resolution images of hydrologic structures in the uppermost regions of the ocean.

[10] This study places particular emphasis on the observation of the seasonal thermocline, as it is a convenient benchmark structure for the exploration of the technical feasibility of shallow SO: the seasonal thermocline features an intense vertical temperature gradient, and is located in our depth range of interest (0–100 m) while ubiquitous geographically. However, this method is not restricted to this target, and is applicable to the study of other structures depending on the area investigated.

[11] This paper is divided into four main sections. Section 2 provides a background to seismic imaging as applied to physical oceanography. It includes an overview of the general features of the seasonal thermocline in the North Atlantic Ocean and in the western Mediterranean Sea, the SO acquisition in general, sources of acoustic noise and their effects, seismic data processing and the general requirements for a SO experiment with an example from a shallow data set. Section 3 presents the four existing data sets examined in detail in section 4, in which the feasibility of the MCS application for shallow ocean observation is examined, and recommendations for an optimal acquisition setup are given. Section 5 outlines our design of the seismic device customized to shallow oceanographic structures using a test case from the western Brittany continental shelf. Finally, we draw conclusions about shallow SO and offer recommendations for future research.

## 2. Seismic Imaging of Shallow Oceanographic Structures

[12] First, we examine the general characteristics of the seasonal thermocline with regard to typical depths, thicknesses, temperature contrasts and reflectivity, in order to provide a general overview of the benchmark structure used in this study. The following subsections are dedicated to the presentation of the seismic reflection measurement, in order to highlight the issues associated to the observation of shallow oceanographic structures, and to define the key parameters for the design of a dedicated seismic acquisition system. Post-acquisition processing aspects are also discussed.

### 2.1. General Overview of the Seasonal Thermocline

[13] In the ocean, at middle and subtropical latitudes, from spring to autumn, a seasonal thermocline forms and separates the warm mixed upper waters, of temperature similar to the surface, from the underlying colder levels [Pickard and Emery, 1990]. The thickness of this thermocline ranges from a few meters to several tens of meters according to the season. The most stratified waters occur during the summer months, and in that time, the thermocline layer becomes the thinnest and the shallowest [De Boyer Montégut *et al.*, 2004]. The thermocline depth and vertical temperature gradient are highly variable, and depend on the latitude [Monterey and Levitus, 1997] and the local conditions of hydrodynamics and sea-atmosphere exchanges [Reygondeau and Beaugrand, 2011]. In general, the temperature contrast between the surface mixed layer and the deeper waters is

on the order of a few degrees Celsius [Pickard and Emery, 1990]. Considering now our areas of interest, the north eastern European shelf is known to display a strong seasonal stratification, which can locally reach 10°C [Puillat et al., 2004]. The top of the seasonal thermocline is typically located at depths between 25 and 45 m [Jurado et al., 2012]. In the Tyrrhenian Sea, similar stratification strength can be found [Small et al., 2012], and depths as shallow as 15–30 m are reached as early as May [D’Ortenzio et al., 2005]. At the other extreme, off the coasts of Florida, the top of the seasonal thermocline occurs deeper, around 100 m in November [SAIC, 1992].

[14] In order to estimate a range of acoustic reflectivity for the seasonal thermocline, temperature profiles acquired during the summer months by ARGO floats at subtropical and middle latitudes (20–45° N) in the North Atlantic Ocean were sampled from the Coriolis data center (Figure 1a; see Table A1 in Appendix A for precise locations of ARGO floats). The selected temperature profiles show various forms of thermoclines, and are in good agreement with the typical mean profiles described by Pickard and Emery [1990] and Jurado et al. [2012]. Reflection coefficients were computed for the seismic frequency range 50–500 Hz, using equation (1) and following the method detailed in section 3. Results plotted in Figure 1b show that the thermocline reflection coefficients vary between –87 and –59 dB, and span the range of the typical reflectivity of oceanographic structures [e.g., Holbrook et al., 2003; Mirshak et al., 2010]. These reflection coefficients are low compared to those typically found in the solid Earth (–40 dB) and at the seafloor (–20 to –8 dB) [Telford et al., 1990]. Reflectivity of the thermocline is controlled by its thickness and the overall temperature contrast between the warm surface waters and the colder underlying levels. In the most stratified waters, reflection coefficients are on the order of –85 to –75 dB at 500 Hz, and of –70 to –65 dB at 100 Hz, but may be as low as –88 dB at 500 Hz and –75 dB at 100 Hz for less prominent thermoclines.

## 2.2. Seismic Oceanography Acquisition Background

### 2.2.1. Source

[15] The energy release of the source is one of the most crucial aspects of seismic acquisition aiming to image weakly reflective oceanographic structures such as the thermocline. The energy budget of a given seismic experiment can be expressed using the sonar equation [Lurton, 2002], applied to the propagation of the seismic signal in the water column:

$$S_1 = S_0(f) + R(f, \theta) - 20 \log_{10}(d_{\text{STG}}) + G_S(f, \theta) + G_R(f, \theta) \quad \text{in dB} \quad (3)$$

with  $S_1$  the sound level recorded by the receiver (in dB re 1  $\mu\text{Pa}$ ),  $S_0$  the source strength (in dB re 1  $\mu\text{Pa}$  @1 m),  $f$  the frequency of the seismic signal,  $R$  the reflectivity of the target (in dB), and  $\theta$  the incidence angle.

[16] In the ocean, the transitions between water masses with different physical properties consist of gradient layers, up to tens of meters thick. The thickness of the “gradient” boundary induces a frequency dependence of the seismic reflectivity. Acoustic waves with long wavelengths, with respect to the gradient layer thickness, see the change in properties as an abrupt step, and thus with the full acoustic

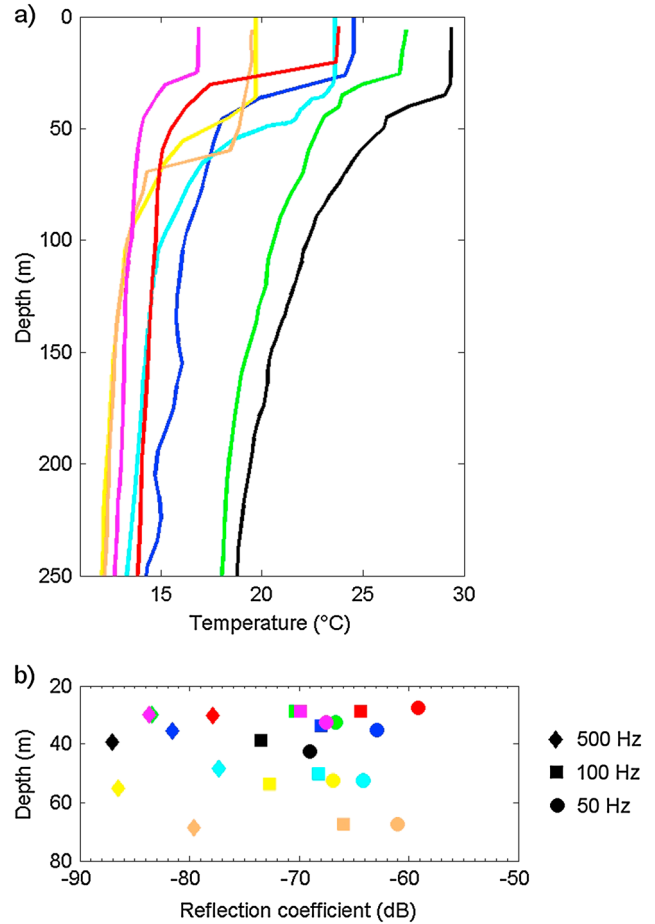


**Figure 1.** (a) ARGO temperature profiles from the CORIOLIS database used to assess the reflectivity of the seasonal thermocline at subtropical and middle latitudes in the North Atlantic Ocean in summer. (b) Corresponding reflection coefficients.

impedance difference. Conversely, shorter waves become sensitive to the details in the gradient layer structure, and effectively decompose it in a succession of smaller jumps. Diffraction effects can arise, due to the interference of waves reflected at different levels inside the gradient layer. For a given situation, the higher the seismic signal frequency is, the lower the reflectivity of the thermohaline structure will be [Hobbs et al., 2009].  $d_{\text{STG}}$  (in meters) is the source-target-receiver distance traveled by the wave, and accounts for the spherical divergence amplitude attenuation. The spherical divergence effect, undergone by any propagating signal, is an important parameter in the seismic acquisition, as the propagation loss it generates is significant at target depths.  $G_S$  and  $G_R$  are frequency and incidence angle-dependent factors which take into account the interference effects of the source and the receiver ghosts. Indeed, the seismic signal results from the sum of two contributions: (i) the “direct” signal, which propagates from the source to the target, or from the target to the receiver; and (ii) the signal reflected by the sea surface (ghost), of reversed polarity and same amplitude as the direct signal. Both  $G_S$  and  $G_R$  range between extinction and +6 dB.

[17] Within this sonar equation,  $R$  and  $d_{\text{STG}}$  are fixed characteristics of the target structure. The source strength  $S_0$  is the only degree of freedom, and it therefore becomes a key parameter: the higher the source emission, the better the thermohaline structure can be imaged. Additionally, the sonar equation highlights the importance of the source frequency, on which depend both the gain associated with the ghost effects, and the reflectivity of oceanographic structures.

[18] The convolutional model of the seismic data [e.g., *Yilmaz, 1987*] expresses the dependence, on the source wavelet characteristics  $w(t)$ , of the amplitude of reflections  $s(t)$  of a seismic wave on a physical interface. To a first approximation, it can be expressed as

$$s(t) = R(t) * w(t) \quad (4)$$

[19] An assumption for this model is that the propagation medium consists of horizontal layers of uniform physical properties. In such a medium and with a signal of given wavelength  $\lambda$  propagating vertically downward, layers that are thinner than  $\lambda/4$  cannot be distinguished by the seismic wavelet [*Widess, 1973; Yilmaz, 1987; Hobbs et al., 2009*]. For a typical seismic frequency range (30–1000 Hz), theoretical vertical resolutions vary between 12.5 and 0.4 m. Consequently, thermohaline fine structure having a vertical scale of around 10 m should be visible using MCS.

[20] In addition, in the Fourier domain, the seismic signal  $S(f)$  produced by the reflection of the source wavelet  $W(f)$  on a gradient boundary  $G(f)$  is defined by

$$S(f) = W(f) \times G(f) \quad (5)$$

[21] The gradient boundary  $g(t)$ , being the integral of the edge function, one may write

$$\text{sinc}(f) = i \times f \times G(f)$$

And therefore,

$$S(f) = W(f) \times \frac{\text{sinc}(f)}{i \times f} \quad (6)$$

[22] As a result, the gradient structure of seawater physical properties induces a low-pass filtering effect on the seismic signal, as observed by *Géli et al. [2009]* on seismic data.

### 2.2.2. Receiver

[23] Another consequence of the low reflectivity of the target is that its imaging with a seismic system will also depend on the sensitivity of the receiver sensor—the hydrophone. The output voltage level of this transducer is defined by the relation

$$U_{\text{trace}} = S_h + S_1 \quad (7)$$

where  $U_{\text{trace}}$  is the voltage level, in dB re 1 V,  $S_1$  is the acoustic pressure level at the hydrophone (in dB re 1  $\mu\text{Pa}$ ), and  $S_h$  is the hydrophone sensitivity, in dB re 1 V/1  $\mu\text{Pa}$ . In the frequency range of interest, the sensitivity of the transducer is omni-directional. In order to introduce directivity, a group of hydrophones, i.e., an antenna—also called seismic trace or channel—is used. The signal resulting from the sum of the antenna sensors is attenuated at the highest

frequencies when incidences are far from vertical. The antenna filter attenuates horizontal noise, while keeping the near vertical reflected waves. Nevertheless, this filter becomes an issue when imaging superficial structures, for which grazing incidences are commonly reached. Thus, while designing a seismic system dedicated to the study of the upper levels of the ocean, special care must be accorded to the source-receiver offsets, as well as to the receiver's antenna specifications. The directional gain of the receiver antenna is proportional to the hydrophone spacing and to the number of sensors [*Krim and Viberg, 1996*]:

$$\text{Att} = 20 \times \log_{10} \left[ \frac{\sin\left(\frac{2n \times 2\pi \times f \times \Delta \times \sin(\theta)}{2v}\right)}{\sin\left(\frac{2\pi \times f \times \Delta \times \sin(\theta)}{2v}\right)} \right] \quad (8)$$

where  $n$  is half the number of hydrophones,  $\Delta$  the distance between hydrophones,  $f$  the signal frequency, and  $\theta$  the incidence angle.

[24] The voltage level exiting the seismic trace being naturally low, a gain is imposed through a pre-amplifier, in order to supply the analog/digital converter with a well-suited amplitude signal. Finally, the use of several antennas combined into a multichannel streamer allows the systematic imaging of each point of the section multiple times, therefore insuring the redundancy of data, and making possible their summation during post acquisition processing.

### 2.3. Acoustic Noise

[25] In the previous sections, the seismic acquisition was considered within an ideal noise-free environment. In reality, noise generated by a variety of processes decrease the performance of the acoustic system. In the typical frequency range used by SO, noise characteristics vary widely depending on technical, geographical, and meteorological factors. The most significant contribution comes from the acquisition system itself as well as the vessel. Imperfections in the source device introduce differences in the source waveform transmitted at each shot (sparker), or produce unwanted secondary signals during the receiving window (airgun “bubble”). The receiver array generates turbulent pressure fluctuations, and the breaking of waves on the seismic device creates noise that propagates mechanically along the streamer. The ship's engines can also produce high levels of noise, particularly at the channels closest to the receiver. For instance, measurements conducted near the 74 m long French R/V *Thalassa* sailing with a 105 rpm engine rotational speed indicate noise levels ranging from 120 to 150 dB re 1  $\mu\text{Pa}/\sqrt{\text{Hz}}$  @ 1 m between 100 and 1000 Hz.

[26] In some particular cases, local or remote shipping activity can also contribute to a significant ambient noise level. *Chapman and Price [2011]* estimated sound levels at about 90 dB re 1  $\mu\text{Pa}/\sqrt{\text{Hz}}$  for remote sites of the Northern Pacific Ocean in 1986 at 40 Hz, with a roughly 20 dB/decade decrease to 500 Hz. At the other extreme, noise levels can be as high as 100 dB re 1  $\mu\text{Pa}/\sqrt{\text{Hz}}$  at 100 Hz at the entrance to the English Channel, arguably one of the busiest worldwide shipping lanes [*Merchant et al., 2012; Stephan et al., 2012*]. Measurements of the noise level generated by wind through the breaking of waves indicate a much lower overall

influence (levels  $< 45$  dB re  $1 \mu\text{Pa}/\sqrt{\text{Hz}}$ ) [Chapman and Price, 2011], while it is generally accepted that rain has a weak impact for sub-kHz frequencies [Chapman and Cornish, 1993].

[27] Finally, significant noise can originate due to multiple reflections from the seafloor originating from the previous shots: if the shot interval is not properly optimized for seafloor topography, the multiple can interfere with the seismic signal. Nevertheless, for shallow targets such as the seasonal thermocline, the recording window is very short and can be squeezed between the sea bottom multiples by setting the shot interval properly. Furthermore, in the particular case of shallow areas, multiples occurring after a shot interval have experienced many reflections at the seafloor, and are strongly attenuated.

## 2.4. Seismic Data Processing

[28] Fundamental to seismic imaging is signal/noise (S/N) ratio enhancement. This ratio is naturally low for SO, due to the weak reflectivity of the target, significant signal propagation loss (although, relative to the solid Earth, water is a rather low-loss medium because of the lack of energy dissipation from shear waves), and the high level of noise in the ocean. For these reasons, careful processing of the seismic data is essential, and, as we will show, the use of a multichannel receiver is also crucial. As the primary objective of this study is to determine the feasibility of the MCS application for shallow ocean observation, only qualitative aspects of processing are addressed in this paper. For this purpose, a basic processing sequence is discussed, including five usual steps—signal processing, data sorting, NMO correction, stack and migration [Yilmaz, 1987].

[29] 1. In order to attenuate very high and very low frequency noise, a band-pass filter is applied. Furthermore, since the high energy direct arrival, propagating horizontally at the sea surface between the source and receivers, masks the shallowest levels of the ocean, specific processing is required. A singular value decomposition (SVD) filter efficiently suppresses the direct wave, the most energetic event of the whole water column: for each common offset gather, after horizontalization of the direct wave, the corresponding first eigenvalues are removed.

[30] 2. The seismic recordings are sorted into common mid-point (CMP) gathers. To enhance the stack efficiency, super CMP gathers are used to increase the seismic fold. This introduces an additional filtering effect, but the sampling remains nonetheless adequate for the horizontal wavelength of the oceanographic structures, on the order of 100 m.

[31] 3. For each CMP, the effect of the source-receiver offset on the seismic signal arrivals is compensated by using an NMO (normal moveout) correction. In order to align arrivals of a given event on the seismic traces of a given CMP gather, travel times are corrected using a sound speed model derived from in situ probes (XBTs, eXpendable BathyThermographs) or by iteratively improving the stack response by making fine adjustments to the NMO correction. As a consequence of this, traces are differentially stretched, causing a significant frequency distortion at shallow depths and large offsets [Yilmaz, 1987]. The distorted zone is then muted as a function of stretch percentage, usually in the range of 50%–150% of the original (prior NMO) wavelength.

[32] 4. The seismic traces of each CMP are then summed during the stack operation. In order to minimize the antenna filter and the NMO stretch effects, it is generally accepted to take into account only reflections associated with incidence angles less than  $45^\circ$ . The stacking process leads to an increase of the S/N ratio of a  $20 \log_{10}(\sqrt{\text{number of stack contributors}})$  factor [Yilmaz, 1987] because the operation is destructive for the uncorrelated signals of the ambient noise, while being constructive for coherent signals.

[33] 5. Finally, the lateral resolution of the seismic image is increased through a process known as migration, which focuses diffracted energy.

## 2.5. Conclusion: General Requirements for Seismic Imaging of Shallow Oceanographic Structures

[34] The signal propagating in the water column undergoes significant amplitude attenuation, due to spherical divergence (section 2.2.1). Moreover, the reflections produced by the seasonal thermocline are weak (see section 2.1), and the seismic acquisition is conducted in a noisy environment (section 2.3). Therefore, the technical challenge of seismic oceanographic imaging comes down to the S/N ratio issue. The use of a powerful source of energy constitutes a key point (section 2.2.1), as well as the use of a multichannel receiver to provide data redundancy, and to increase the S/N ratio using conventional processing (section 2.4). In addition, the receiver antenna and its resulting directivity allow filtering of horizontal noise provided the incidences remain close to vertical (section 2.2.2). Thus, small incidence angles are crucial in order to avoid attenuation of the signal by the antenna filter. Moreover, amplification of the signal exiting the trace is necessary. Another key point of seismic acquisition is the signal wavelength. It is of primary importance in order to adequately discriminate the thermocline layer, with a thickness as little as a few meters. Finally, dedicated processing must also include the removal of the coherent noise of the direct wave arrival, which masks the shallowest part of the water column.

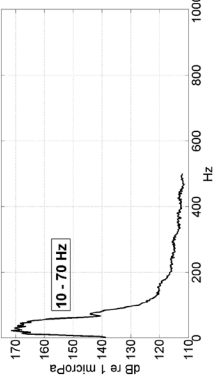
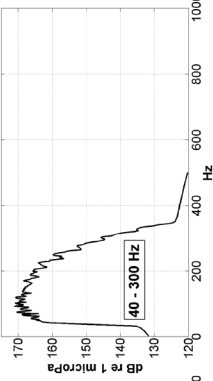
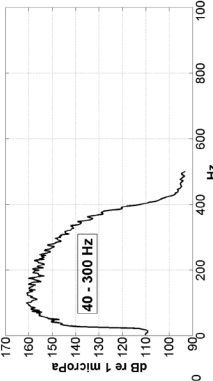
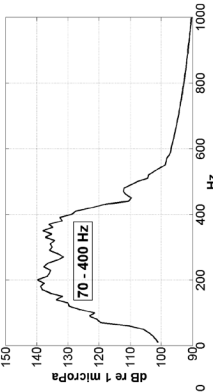
## 3. Examples of Shallow SO Data Sets

[35] In this study, four MCS sections are explored. Data were recorded during three independent scientific cruises:

[36] 1. GO (Geophysical Oceanography) was an EU-funded project conducted during March and April 2007 using the British RRS Discovery and German FS Poseidon in the Gulf of Cadiz (NE Atlantic). This cruise was dedicated to the mostly deep seismic oceanographic imaging of the Mediterranean Outflow Water (MOW) into the Atlantic [Géli et al., 2009; Hobbs et al., 2009; Sallarès et al., 2009; Quentel et al., 2010]. Repeated transects were conducted using different sources—low, medium and high resolution—which provided a range of frequency contents and source strengths, while capturing the upper thermohaline structure. Two GO seismic sections are analyzed in this study.

[37] 2. The Carambar survey [Mulder et al., 2011, 2012a, 2012b] was led by the University of Bordeaux (T. Mulder, EPOC) onboard the French vessel R/V Suroît, and took place in November 2010 in the Florida Straits (Bahamas Plateau). Its primary geological objective was to characterize

**Table 1.** Acquisition and Processing Parameters for the Go, Carambar and Sigolo Seismic Sections, and Characteristics of the Oceanographic Targets Seismically Mapped

SOURCE	GO-LR	GO-HR	CARAMBAR	SIGOLO
Type	Two arrays of three Bolt 1500 LL airguns at a distance of 3 m. Total volume: 2320 ci	Two arrays of three SODERA MiniGI at a distance of 10 m. Total volume: 117 ci	MiniGI 24/24 ci	Sparker SIG 250 J
Tow depth	8 m	1.5 m	1.5 m	2 m
Average shot spacing	50 m	35 m	8 m	15 m
Source strength	233 dB re 1 $\mu$ Pa @ 1 m	218 dB re 1 $\mu$ Pa @ 1 m	209 dB re 1 $\mu$ Pa @ 1 m	192 dB re 1 $\mu$ Pa @ 1 m
Amplitude spectrum				
<b>RECEIVER</b>	SERCEL SEAL LR	SERCEL SEAL HR	SERCEL SEAL HR	SERCEL SEAL HR
Type	8 m	2 m	2 m	2 m
Tow depth	192	72	96	72
Number of channels	12.5 m	6.25 m	6.25 m	6.25 m
Group spacing				
<b>GEOMETRY</b>				
Source-first trace offset	122 m	94 m	32 m	32 m
Ship-first trace offset	155 m	105 m	50 m	78 m
<b>CHANNEL SPECIFICATIONS</b>				
Number of hydrophones	16	8	8	8
Hydrophone spacing	0.625 m	0.78 m	0.78 m	0.78 m
Sensitivity	-195 dB re 1 V/1 $\mu$ Pa	-196 dB re 1 V/1 $\mu$ Pa	-196 dB re 1 V/1 $\mu$ Pa	-196 dB re 1 V/1 $\mu$ Pa
<b>AMPLIFIER</b>				
Gain	0	12 dB	12 dB	12 dB
<b>PROCESSING</b>				
Bin size	25 m	25 m	25 m	25 m
Mean fold	95	79	215	70
Mute of NMO distorted signals: maximum stretch	100%	100%	50%	150%
<b>STRUCTURES IMAGED</b>				
Structure, depth, XBT derived reflection coefficient	Previous winter mixed layer base, 115–140 m, -91 dB	Thermocline, 50–75 m, -85 dB Previous winter mixed layer base, 115–150 m, -87 dB	Overflow, 52–110 m, -89 to -77 dB	Thermocline, 10–40 m, -85 to -74 dB

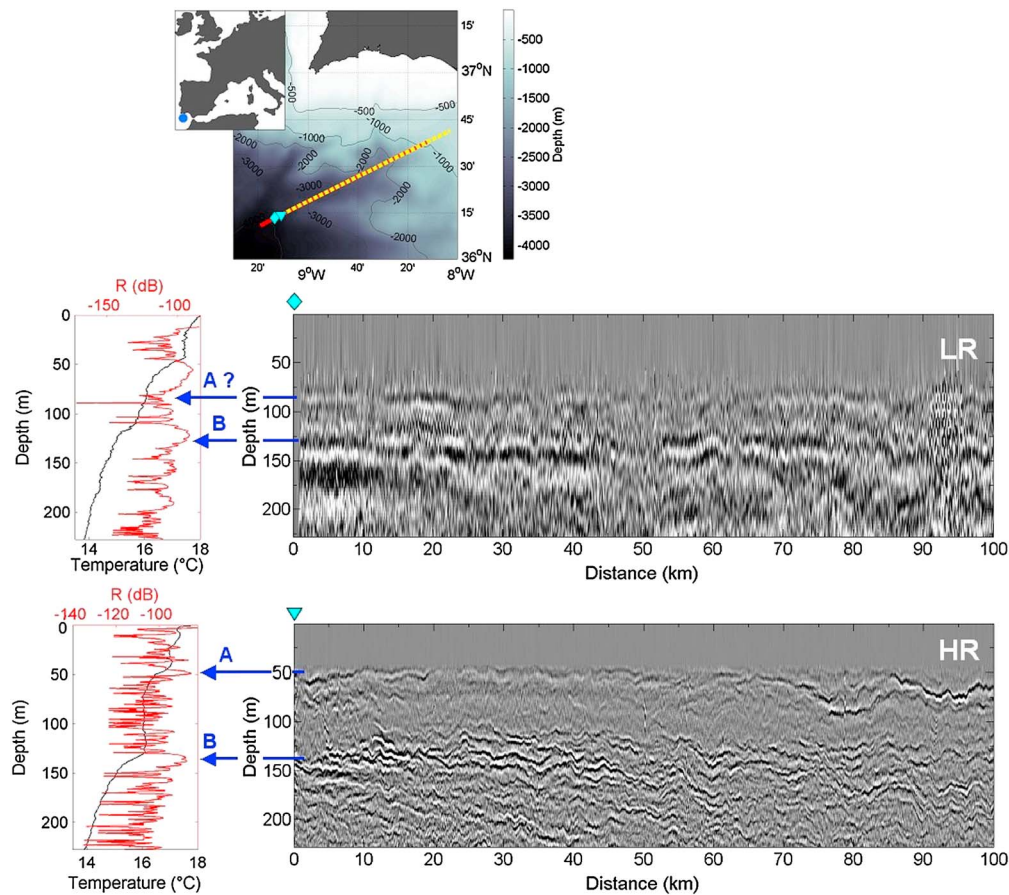


**Figure 2.** (top) Bathymetric map of the GO study area and coincident seismic and hydrological data positions. The red line indicates the GO-LR #01 seismic section, acquired on 1–2 May 2007 and the dotted yellow line the GO-HR #13 section, acquired on 9–10 April 2007. The light blue markers indicate the XBT positions, acquired simultaneously with the seismic data: the triangle for GO-HR #13 and the diamond for GO-LR #01. The inset shows the geographic setting of the study region, indicated by the blue dot. (middle left) GO-LR #01 XBT temperature profile (black) and derived reflectivity (red). (middle right) Processed GO-LR #01 seismic section. Data processing details are outlined in text. The position of the XBT station is indicated by the light blue diamond. The section features the remnant layer base (arrow B), at depths between 115–140 m, and a reflector at 85–100 m depths that can be interpreted either as the base of the thermocline (arrow A), or possibly as an artifact of the direct wave. (bottom left) GO-HR #13 XBT temperature profile (black) and derived reflectivity (red). (bottom right) Processed GO-HR #13 seismic section. Data processing details are outlined in text. The position of the XBT station is indicated by the light blue triangle. The section features the seasonal thermocline (arrow A) at depths between 50 and 75 m, and the previous winter mixed layer (arrow B) at depths between 115 and 150 m.

the geometry of the Bahamas carbonate slope system and its relationship to sedimentary processes. This seismic survey also captured the thermocline signal in the upper part of the water column.

[38] 3. The Sigolo survey was led jointly by Exxon, Total and Ifremer and took place in June 2008 along the East-Corsica margin (Tyrrhenian Sea) onboard the R/V Suroît [Jouet *et al.*, 2011; Calvès *et al.*, 2012]. Its geological purpose was to map the architecture of the sediments in the Golo fan, and each of the deposit environments from the Golo river to the basin. Seismic sections also feature shallow ocean reflectors associated with the seasonal thermocline.

[39] In this manuscript, we follow oceanographic conventions and use the term profile for a one-dimensional measurement or data set along the vertical (depth) axis and the term section for a set of horizontally consecutive profiles.

Thus, for example we may refer to a CTD or XBT profile and a 2D seismic section. The respective terminology in seismology would be stacked trace and profile, respectively.

[40] The four seismic sections supplied images of varying quality regarding superficial hydrological structures. They allowed exploration of the technical feasibility of shallow seismic oceanography using four different acquisition setups. Acquisition parameters are listed in Table 1. Spectra of the amplitudes of the source signals were computed by taking the average spectra of seafloor and sediment reflections from processed data. The theoretical vertical resolution was defined for the central source frequency and a sound speed of 1500 m/s based on the Rayleigh criteria (see section 2.2.1). Source strengths were estimated using seismic data because no direct measurement was performed during the three cruises. For each acquisition, the source strength  $S_0$

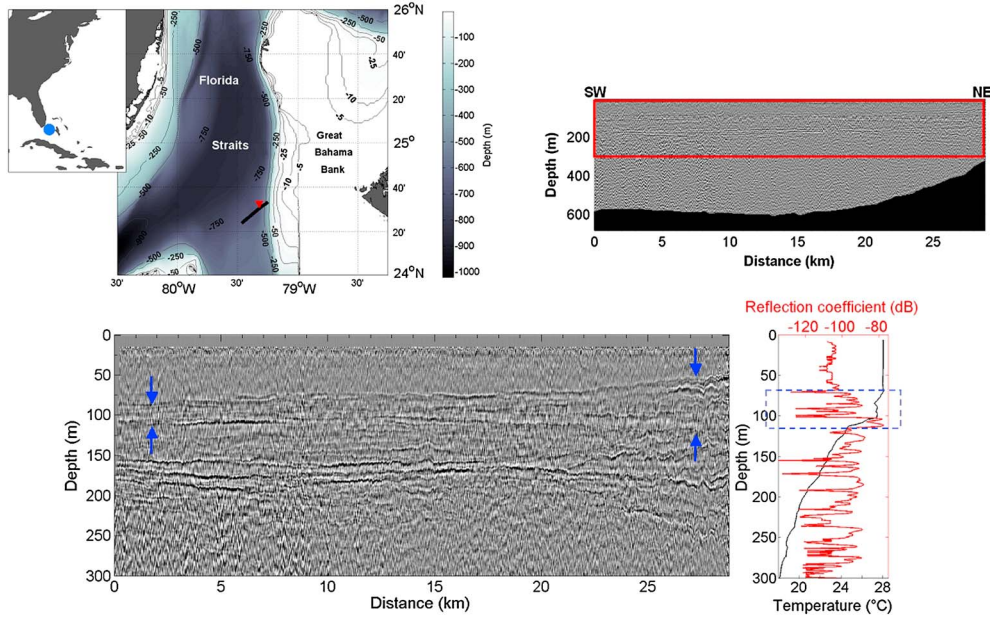


**Figure 3.** (top left) Bathymetric map of the Carambar study area showing seismic and hydrological data positions. The black thick line shows the location of Carambar seismic section #14, acquired on 9–10 November 2010, and the red triangle the XBT station acquired on 5 November 2010. The inset shows the geographic setting of the study region, indicated by the blue dot. (top right) General overview of the processed seismic section #14. Data processing details are outlined in text. The red box denotes the enlarged portion of the profile presented below. (bottom left) Enlarged view of the processed section #14. Reflectors at depths ranging from 52 to 110 m are the signature of an overflow from the neighboring Grand Bahama Bank, which gets thinner further from the bank. The blue arrows indicate the top and the bottom boundaries of the structure. (bottom right) XBT temperature profile (black) and derived reflectivity (red). The dashed blue box indicates the extent of the overflow.

was calculated using the following equation derived from Warner and McGeary [1987]:

$$S_0 = 20 \log\left(\frac{2za_1}{R}\right) - 12 \text{ in dB re } 1\mu\text{Pa}@1 \text{ m} \quad (9)$$

$$\text{with } R = 2 \times \frac{a_2}{a_1} \quad (10)$$

where  $R$  and  $z$  are respectively the reflection coefficient and the depth of the seafloor. The variables  $a_1$  and  $a_2$  are the amplitudes of the seafloor reflection and seafloor first multiple, respectively picked on a high S/N common offset gather, using the envelope of the signals. Reflection points are assumed to be identical for both the seafloor and its first multiple, and the travel distance for a reflection on the sea bottom is assumed to be exactly half its first multiple travel distance. Thus, this method is applied on a short offset receiver with normal incidence on the seafloor. The  $-12$  dB in equation (9) is an empirical value, which takes into account the source and receiver ghost effects for the ideal case of normal incidence and constructive interference (see section 2.2.1). This method is based on approximations; for instance, it does not take into account that the source and receiver are towed at variable depths. Nevertheless, estimated source strengths are consistent with stated manufacturer data, wherein the orders of magnitude for this parameter are provided. Further calculations presented in section 4 include the quantification of the antenna filter induced attenuation performed using equation (8) (see section 2.2.2), and the estimation of the mean noise

level using the seismic data. In this case, for each single channel recording, the mean of the envelope amplitudes inside a window above the direct wave was computed, then, values from all the channels were averaged.

[41] Figures 2–4 present the four processed seismic sections. The processing sequence included the following steps: band-pass filtering, direct wave removal, noise editing (for Sigolo), NMO correction, stacking and post-stack phase-shift migration. For the NMO correction, an average constant sound speed derived from XBT data was used. Although it is an approximation [Fortin and Holbrook, 2009], this simplified model allows a sufficient S/N ratio for the stack. The same sound speed is used for the migration, and to convert time outputs to depths.

[42] Acoustic reflectors and actual physical properties of the seawater from XBT data were correlated. During the Sigolo and GO cruises, these temperature measurements were conducted simultaneous to the seismic survey, while in the Carambar case, one XBT was cast in the vicinity of the studied seismic section, 2.7 miles to the north and 5 days apart from the seismic experiment (Figure 3). In this case, temperature measurements are in good agreement with former studies performed during the same season [Wennekens, 1959; SAIC, 1992; Leaman et al., 1995], suggesting that it is indeed representative of the hydrological structure sampled by the seismic survey.

[43] In the three oceanographic contexts investigated, reflectivity of the upper layer of the water column is mostly controlled by temperature. Study of the following: (i) in the



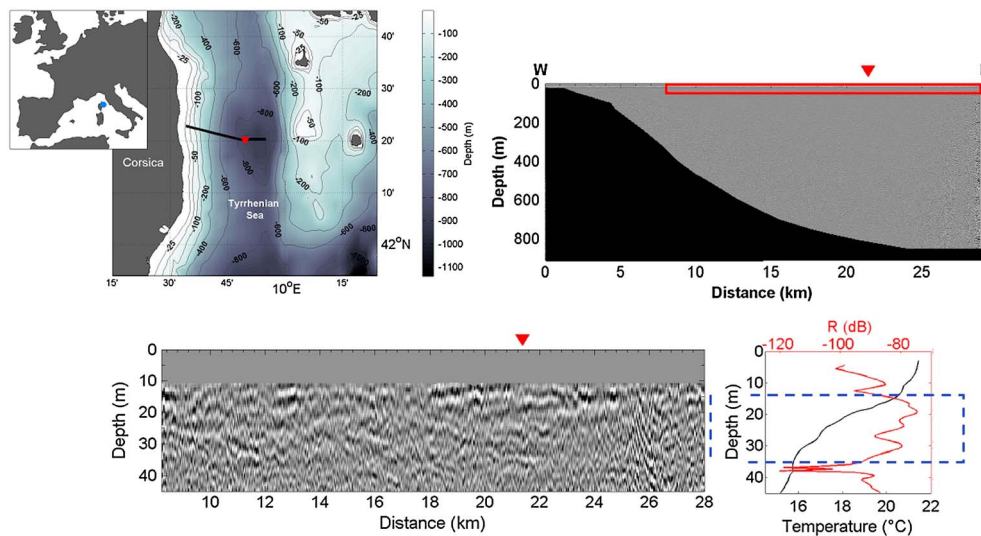


**Figure 4.** (top left) Bathymetric map of the Sigolo study area and coincident seismic and hydrological data positions. The thick black line features Sigolo seismic section #9 acquired on 12 June 2008 from 18:30 to 21:40 UT, and the red triangle is the XBT station acquired the same day at 19:20 UT. The inset shows the geographic setting of the study region, indicated by the blue dot. (top right) General overview of the processed seismic section #9. Data processing details are outlined in text. The red box denotes the enlarged portion of the section presented below. The red triangle indicates the position of the XBT station. (bottom left) Enlarged view of processed section #9. The position of the XBT station is indicated by the red triangle. Reflectors at depths ranging from 10 to 40 m are the signature of the seasonal thermocline. (bottom right) XBT temperature profile (black) and derived reflectivity (red). The dashed blue box indicates the extent of the seasonal thermocline.

GO cases, CTD stations in parallel of XBT, and (ii) for Carambar and Sigolo, historical data [SAIC, 1992; Vetrano *et al.*, 2010], showed that in the three areas investigated, in the 0–200 m layer, the salinity contrast is on the order of 0.5 psu, while the XBT data demonstrates a 3 to 8°C temperature contrast. In addition, for the Carambar and Sigolo cases, comparison of the acoustic impedance variations produced respectively by temperature and salinity gradients showed that the salinity contribution represents ~7% of the temperature contribution. For the GO case, computation of the reflection coefficient using a constant salinity yields a relative error smaller than 20%. Therefore, for the calculation of the reflectivity in this study, salinities were considered as constant vertically using the following: (i) for GO, the average results obtained from the CTD stations; (ii) for Sigolo and Carambar, measurements of salinity with the ship-board thermosalinometers during the seismic acquisition.

[44] Since reflectivity is frequency dependent (see section 2.2.1), the temperature profiles were subsequently smoothed by a  $\lambda/4$  window moving average, in order to introduce the source vertical resolution effect in the estimation of reflectivity. Reflection coefficients  $R$  were then calculated for vertical incidence using equation (1).

[45] Below, we describe the local oceanographic features that will be used as benchmarks in the following technical study (section 4). Their parameters—depth and XBT derived reflection coefficient—are listed in Table 1.

[46] (a) *GO—Gulf of Cadiz*. Here, we explore the LR01 and HR13 sections recorded along the same transverse using two different seismic configurations: the first one using a low-resolution (LR) source and the second one using a high-resolution (HR) source (see Table 1), performed 10 days apart.

The LR and HR seismic images of the shallowest levels of the water column are presented in Figure 2. The XBT data exhibit little change in the thermohaline structure between the two acquisitions. In the HR section, discontinuous reflectors indicated by arrow A image the thermocline (Figure 2). A second group of reflectors identified by arrow B is interpreted as the bottom of the previous winter mixed layer (remnant layer). This structure is present as well on the LR section (arrow B, Figure 2).

[47] (b) *Carambar—Bahamas Plateau*. The section presented in Figure 3 displays a highly reflective zone located at depths between 50 and 190 m. We identified the upper part of this zone as being an overflow, i.e., a dense water plume sinking from the neighboring Grand Bahama Bank into the Florida Straits [Hickey *et al.*, 2000]. In the XBT temperature profile, the eroded base of the mixed layer is the signature of this plume.

[48] (c) *Sigolo—East-Corsica Continental Margin*. Very shallow structures can be identified as illustrated in Figure 4. A high reflectivity zone is located at depths between 10 and 40 m. Based on its depth, we interpreted this as the signature of the seasonal thermocline.

#### 4. Lessons on SO From the Examined Shallow Water Data Sets

[49] In the four seismic sections explored in this paper thus far, superficial oceanographic structures such as the seasonal thermocline (GO-LR and HR, Carambar and Sigolo), an overflow (Carambar) and a remnant layer (GO-HR) have been mapped with reflectors located at depths ranging from 10 to 150 m. Here, the four surveys are analyzed and

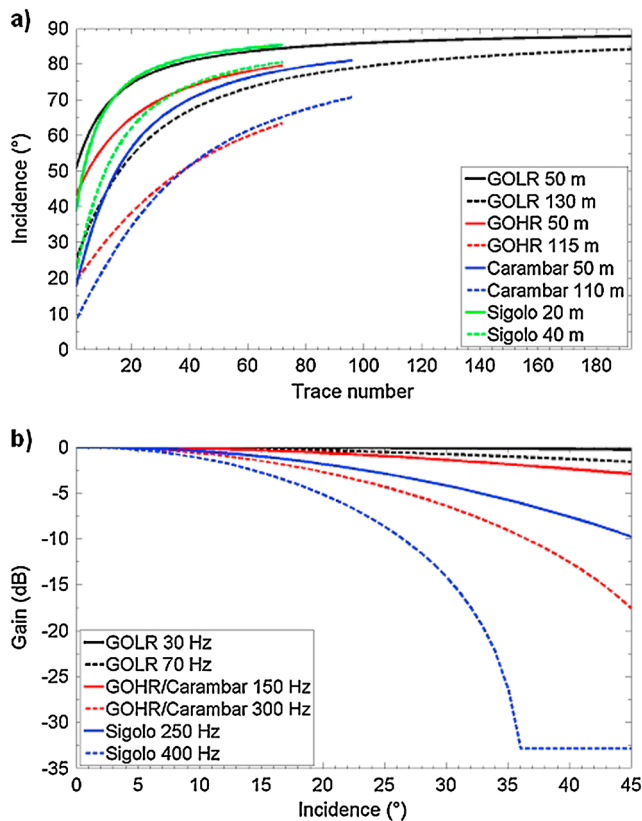


**Figure 5.** (a) Incidence angles associated with the main reflectors of the GO, Carambar and Sigolo seismic sections. (b) Antenna filter induced attenuation for GO, Carambar and Sigolo frequency contents. Solid lines in the graph outline the central frequency of each spectrum, and dotted lines its upper limit.

compared. The quality of the images of superficial hydrological structures is variable. Influence of the acquisition parameters are explored and quantified in order to provide benchmarks for the definition of optimal configurations for seismic imaging of the seasonal thermocline and shallow water data sets in general. Processing aspects are also discussed. All acquisition parameters are listed in Table 1.

#### 4.1. Low Frequency Seismics: The GO-LR #01 Section

[50] As demonstrated in section 2, an important keystone of seismic imaging of weakly reflective oceanographic structures is the use of highly energetic sources. In the first case study, the seismic line GO-LR #01 was acquired using a powerful source constituted of six large volume airguns (see Table 1, column 2). The associated source strength was high: 233 dB re  $1 \mu\text{Pa}$  @ 1 m. The direct arrival is very strong and masks the whole superficial part of the water column in the raw data. The SVD filter allowed elimination of most of this signal, with some residual artifacts still affecting the shallowest parts of the processed image as seen on Figure 2. Indeed, in this image, the discontinuous low amplitude reflector located from 85 to 100 m depths (Arrow A, Figure 2) can barely be interpreted. It may be correlated with the base of the thermocline detected on the XBT profile, or alternatively could be interpreted as an artifact of the direct wave. On

the other hand, the seismic signal of the base of the remnant layer can clearly be identified (Arrow B, Figure 2). Nevertheless, the resolution is low: the reflectors appear thick and blurry on the section, due to the 13 m vertical resolution of the GO-LR source. Furthermore, the large offset between the source and the receivers ( $\geq 122$  m, see Table 1), implies high incidence angles. Figure 5a illustrates that, for a 50 m deep thermocline, a  $51^\circ$  incidence angle is reached at first trace. In the case of the deeper remnant layer base reflector, around 130 m deep, the  $45^\circ$  incident angle limit is reached at the 12th trace. In spite of these high incidences, the antenna filter effect is negligible due to the low frequency content, as shown in Figure 5b. The relevant conclusions that can be drawn from this experiment are that the GO-LR #01 setup features strong limitations for the imaging of fine scale and superficial thermohaline structure. The large offsets are ill-suited for imaging shallow structures, as well as the very low frequency source, which does not offer high resolution of thin ( $\sim 10$  m) target layers.

#### 4.2. High Frequency Seismics: The GO-HR #13 Section

[51] This section was acquired using a high-resolution seismic system, featuring a central source frequency of 150 Hz, having a vertical resolution of 2.5 m. (see Table 1, column 3). As a result, the processed section (Figure 2) provides a considerably more detailed image of the thermohaline fine structure. It also shows that the direct wave was efficiently suppressed. The correlation between the thin continuous reflectors and the XBT data is straightforward, and structures mapped by the seismic section can be easily identified. Moreover, although the source strength is 15 dB lower than for the GO-LR section, the processed image features a high S/N ratio. Noise level estimations for each single seismic channel show a marked dependence on the ship's offset, indicating low ocean-induced noise. Accordingly, the thermocline signal appears clearly on the first single channel recordings. As a result, the source power seems well-suited to the imaging of the acoustic target. Furthermore, the GO-HR receiver system is more compact than the system deployed during the LR acquisition. A shorter source to receiver offset was used, and the HR streamer featured channels that are twice as small as for the LR streamer. Consequently, Figure 5a shows that the 50 m deep thermocline can be mapped with incidence angles lower than  $45^\circ$ , while still 30 traces contribute to the stack for the 135 m target. For a given frequency and a given incidence angle, the HR streamer seismic channel has a lower antenna filter effect than the LR streamer. Nevertheless, the higher frequency content of the GO-HR source induces a greater attenuation: for a  $45^\circ$  incidence angle, losses vary between 3 and 17 dB for frequencies ranging from 150 to 300 Hz (Figure 5b).

[52] Comparison of the HR and LR GO acquisitions highlights the necessity of a source of high frequencies—hundreds of Hz—in order to finely image the first 100 m of the water column. It also demonstrated that a good compromise can be found between source strength and vertical resolution. However, the deployment of the two array GO-HR source requires a ship of substantial size, which can be a drawback for coastal studies of the thermocline.

### 4.3. High Frequency, Small Volume Seismic Source: The Carambar #14 Section

[53] The source used for the acquisition of Carambar section #14 is a small volume airgun, with a spectral content similar to the GO-HR source (see Table 1, column 4). In Figure 3, the acoustic image of the overflow is detailed and features thin reflectors showing good continuity along the entire section. As with GO-HR, the SVD filter efficiently suppressed the direct arrival. Nevertheless, the Carambar source strength—209 dB re 1  $\mu$ Pa @ 1 m—is significantly lower than the levels of the previously analyzed sources. The effect of this comparatively low amplitude signal was studied based on a synthetic approach using the XBT data. Using sonar equation (3), the levels of the overflow signals at the hydrophone were calculated, and a mean noise level was estimated using the seismic data and the method presented in section 3. Small differences were found between signal and noise levels: the top and bottom overflow reflections respectively produce an 88 and a 98 dB signal (re 1  $\mu$ Pa), while the mean noise level reaches 105 dB re 1  $\mu$ Pa, indicating poor sea recording conditions. These results are in agreement with the single common offset sections: reflectors are not visible for the first channels and appear at the channel #5, where the ship-induced noise has become low enough. Comparatively, the same calculation using GO-HR #13 XBT data yielded a 106 dB (re 1  $\mu$ Pa) for a thermocline of lower reflectivity and located at the same depth than the Carambar target.

[54] In summary, the S/N ratio of the Carambar processed data is not as high as for GO-HR, due to a noisier environment and a lower source strength. It appears thus that the seismic system deployed during the geological Carambar survey requires optimization for SO purposes regarding the source energy aspect.

### 4.4. High Frequency, Low Energy Sparker Source: The Sigolo #9 Section

[55] Sigolo seismic section #9 was acquired in well-stratified waters, with a thermocline twice as shallow as those detected on the former sections (see Table 1, column 5). This section allows us to address the imaging of very shallow structures with a light, high-resolution seismic source using the same vessel and receiver layout as for the Carambar survey. The Sigolo source was a SIG sparker with a 250 Hz central frequency. The resulting 1.5 m vertical resolution allows fine discrimination of the physical property variations related to the thermocline (Figure 4). Moreover, the short seismic source signature allows the imaging of targets as shallow as 10 m, while, comparatively, the shallowest structure captured by the GO-HR seismic system was located at a 50 m depth. Nevertheless, this sparker source produces a significantly less impulsive signal than the air guns, with a lower source strength of 192 dB re 1  $\mu$ Pa @ 1 m. As a result, the S/N ratio of the stacked image is lower than for the Carambar survey. In addition, in the Sigolo common offset gathers, reflectors of the thermocline feature low amplitudes, and the image is difficult to interpret. The minimal difference between the 99 dB (re 1  $\mu$ Pa) synthetic level of the thermocline signal at the hydrophone (computed using the method presented in section 4.3) and the mean ambient noise (for calculation details, see section 3), of 95 dB re 1  $\mu$ Pa corroborates this observation.

[56] The Sigolo survey was conducted using the same seismic streamer as GO-HR, with the exception of using 24 more channels (96 as opposed to 72). The source to first receiver offset of 32 m was one third the size of the GO-HR offset, providing comparatively lower incidence angles, and an increased number of contributing channels to the stack (Figure 5a). Nevertheless, the source-receiver offset appears too large with regard to the shallow depth (10–40 m) of the thermocline. As illustrated in Figure 5a, only targets located deeper than 16 m feature incidence angles lower than 45°. Moreover, the high frequency content of the signal induces a significant antenna filter attenuation. Figure 5b shows that, for a 45° incidence angle, the losses reach 10 dB at 250 Hz, and the maximum frequency of the spectrum (400 Hz) lies within the lobe of attenuation. In conclusion, while the vertical source resolution and signal length appear to be ideal, the source strength could be improved. Offsets as well as channel specifications of the HR streamer are not optimal for the study of the seasonal thermocline in this oceanographic context.

### 4.5. Conclusion: Optimal Seismic Setups for Imaging Superficial Oceanographic Structures

[57] The quantitative analysis of the GO-LR and GO-HR, Carambar and Sigolo seismic acquisition systems allows us to optimize parameterisation for the design of a seismic system specifically dedicated to the observation of the shallow layers of the ocean.

[58] 1. As demonstrated in section 2, S/N ratio is of prime concern. First, to detect the weak reflections of the water column, a significant ( $> 192$  dB re 1  $\mu$ Pa @ 1 m) source strength is required. However, when choosing a seismic source, the spectral content must be also taken into account. Fine scale thermohaline variations of the superficial waters are captured in greatest detail by high frequency ( $> 150$  Hz) sources. Secondly, in order to increase the S/N ratio and to obtain good quality images, the use of a multichannel seismic streamer (MCS) is essential.

[59] 2. When defining the seismic streamer's parameters and the geometry of the system, the incidence angle issue must also be taken into account. High angles are responsible for both attenuations at high frequencies due to the antenna filter (see section 4.4), and for muting of the NMO-distorted shallowest arrivals during the stack (see section 4.1). The characteristics of the seismic channel play a key role in the antenna filter. When using high frequencies ( $> 250$  Hz), hydrophone spacing smaller than 0.625 m and trace apertures smaller than 6.25 m are essential. Furthermore, because near-vertical incidences allow one to work free of horizontal noise (see section 2), source-receiver offsets must be kept small and must be defined according to the target depth. For example, a 30 m source-first trace distance appears to be too large for the study of a thermocline located at depths between 10 and 100 m.

## 5. Design and Sea Trial of a Seismic System Dedicated to Shallow SO

### 5.1. Imaging of the Shallow Thermocline on the Western Brittany Continental Shelf

[60] In order to validate the resulting specifications of the former analysis, a test case was considered: the seismic

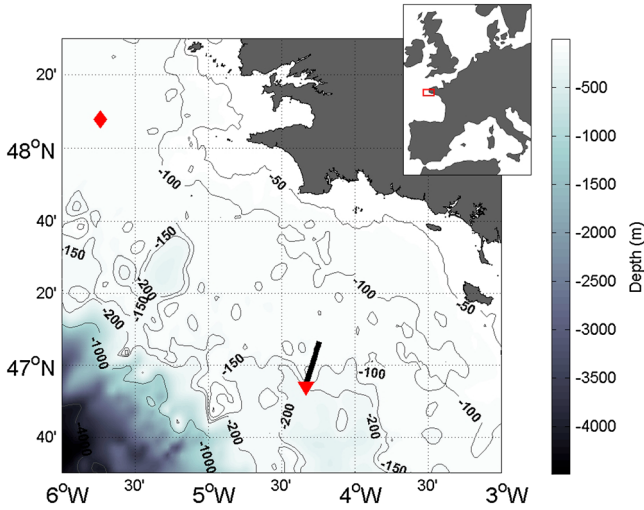


**Figure 6.** Bathymetric map of the western Brittany continental shelf, and positions of seismic and hydrological data from the ASPEX and Fromvar cruises. The red diamond indicates the XBT cast on August 8<sup>th</sup> 2010 during the Fromvar cruise. The black thick line shows ASPEX seismic section #1, and the red triangle indicates the associated CTD station, acquired on the June 17<sup>th</sup> 2012. The inset shows the geographic setting of the study region, indicated by the blue dot.

imaging of the seasonal thermocline on the western Brittany continental shelf (North East Atlantic).

[61] Thermally stratified from April to October, the open waters of the Brittany shelf feature a ~10 m thick, 30 m deep thermocline during the summer months [Le Corre and Mariette, 1985; Le Boyer et al., 2009]. In order to characterize the target, hydrological data were collected during the Fromvar cruise, conducted in this area in early August 2010 aboard the French R/V *Côtes de la Manche* (Figure 6). During this survey, the seasonal thermocline was identified using XBT and CTD probes. Figure 7 features one recorded vertical XBT temperature profile acquired in the area, displaying a typical summer thermocline. The associated reflectivity profile is also plotted. As CTD data showed little variation of the salinity between the sea surface and bottom (< 0.1 psu), the reflection coefficient was computed for a constant mean salinity value (see section 3 for calculation details). Figure 7 illustrates that the transition between the warm surface layer and the colder deep waters occurs through a 15 m thick layer, at depths between 19 and 35 m, with a 7°C overall temperature contrast. The corresponding reflection coefficient is relatively high, on the order of -71 dB for a 400 Hz frequency.

## 5.2. Seismic Acquisition System

[62] The optimal seismic system suited for imaging this seasonal thermocline can be defined using the catalog of seismic acquisition systems analyzed in this paper, and taking advantage of an existing high-resolution seismic system initially tailored to shallow geological 3D seismic surveys.

### 5.2.1. The Source

[63] Analysis of the GO-LR seismic section showed that powerful sources such as airguns are ill-suited to the study of structures that are both superficial and of small vertical

thickness (see Figure 2). The signal is long compared to the short recording window. In addition, residual artifacts of the direct waves are observed after SVD filtering. Thus, a high-resolution source producing a compact signal is required to provide a detailed image of such targets. More particularly, for the imaging of a 30 m deep seasonal thermocline, the seismic source signature must be less than 40 ms long. Furthermore, from a more practical perspective, studies of the seasonal thermocline in the shallow Iroise Sea are most easily conducted aboard small vessels (< 25 m), which therefore necessitate a compact system. Among the four types of sources explored in this paper, the sparker is thus the smallest system, and features the highest frequency content and the shortest signal. In addition, pool tests conducted with a SIG sparker used at a 1000 J energy showed that the source can produce of signal with a 400 Hz central frequency, providing a vertical resolution lower than 1 m. While comparatively low, the source strength of the sparker deployed for the Sigolo acquisition allowed detection of the seasonal thermocline in the Tyrrhenian Sea, with a slightly lower reflectivity than in the Iroise Sea (see Table 1 and Figure 7). Nevertheless, the source strength of the sparker can be increased. During the pool tests, energies ranging from 160 to 5000 J were used, and source strengths as high as 210 dB re 1  $\mu$ Pa @ 1 m were reached. To go further, we used the Fromvar data to provide a benchmark for the source strength required for the detection of the typical Iroise summer thermocline. An ideal noise-free environment and a configuration of constructive interference between the source and receiver ghosts were considered. The following relation, derived from equation (3), was used:

$$S_0 = S_1 - R + 20 \log(d_{\text{STG}}) - 12 \quad (11)$$

where the reflection coefficient  $R$  is -71 dB, and the source-target-receiver distance 60 m. For a level  $S_1$  of 106 dB—the relatively high level produced by the GO-HR thermocline (see section 4.2)—the computed source strength requirement is 198 dB re 1  $\mu$ Pa @ 1 m.

[64] The small ship size prevented us from taking both an airgun and a sparker source. We used the available sparker, which was limited to 1000 J and delivered a source strength of 205 dB re 1  $\mu$ Pa @ 1 m.

[65] With the survey taking place in relatively shallow waters (depths < 200 m, see Figure 6), the shot interval must be carefully defined. A 200 m deep seafloor generates a first order multiple that occurs at 266 ms TWT (two-way travel time). Therefore, taking a shot interval of 2 s insures a seismic image free of any sea bottom multiples from previous shots.

### 5.2.2. The Receiver

[66] At the dominant frequency of the 1000 J sparker source (400 Hz), the induced antenna filter attenuation for the SERCEL SEAL HR streamer is significant (see Figure 5b). This 6.25 m HR streamer trace spacing is therefore too long for the source spectral content. We thus have operated streamers with short hydrophone spacings (0.3 m) and short trace antennae (1.8 m). The attenuation reaches 0.5 dB for a 20° incidence angle, and only 1.5 dB for 45° incidence. Moreover, the source-receiver offsets must not exceed 20 m in order to keep incidence angles smaller than 20° for a 30 m deep thermocline. This limits the number of traces of the receiver.

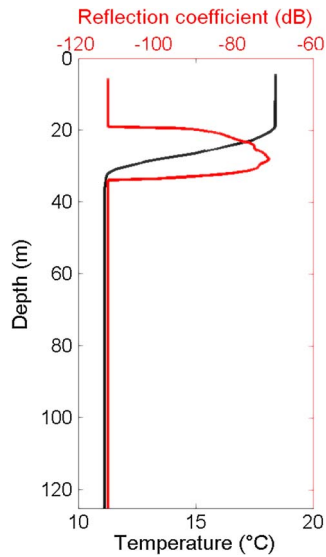


**Figure 7.** XBT temperature profile (black) acquired on 8 August 2010 at the position N48°08–W5°44 during the Fromvar cruise, and associated reflectivity (red).

We used streamers of only six traces and a short offset of 8 m between the source and the first trace. Moreover, a high hydrophone sensitivity of  $-190$  dB re  $1$  V/ $1$   $\mu$ Pa was chosen. Finally, as introduced in sections 2 and 4, a high multiple coverage is crucial to insure a sufficient S/N ratio after stacking. For the Brittany thermocline, with a bin size of 12.5 m, a 2 s shot interval and a 1.8 m trace spacing, a 100-fold coverage requires 24 traces. In order to avoid large offsets while preserving high coverage, a small offset, multiple-streamer seismic device appears to be the best choice. Thus, the following optimal setup can be proposed: (i) four seismic streamers of six 1.8 m long hydrophone groups each; the outer receivers are deployed using booms such that the four streamers are equidistant, 4 m apart; (ii) a 1000J sparker source towed between the two inner streamer cables, 8 m away from the first traces.

### 5.3. Results

[67] The experimental acquisition system was tested in the configuration presented in Figure 8 during the ASPEX cruise (L. Marié, LPO). During this survey, combined seismic acquisitions and CTD measurements were conducted on the western Brittany continental shelf aboard the French R/V Gwen Drez

**Table 2.** ASPEX Seismic Acquisition and Processing Parameters

Source	
Type	Sparker SIG
Power	1000 J
Tow depth	1 m
Shot interval	2 s
Source strength	205 dB re $1$ $\mu$ Pa @ 1 m
Receiver	
Length	10 m
Tow depth	Surface
Number of channels	6
Group spacing	1.80 m
Number of receivers	4
Geometry	
Source-first trace offset	8 m
Ship-first trace offset	28 m
Channel Specifications	
Number of hydrophones	6
Hydrophone spacing	0.30 m
Sensitivity	$-190$ dB re $1$ V/ $1$ $\mu$ Pa
Amplifier	
Gain	39 dB
A/D Converter	
Numerical resolution	16 bits
Sampling rate	125 $\mu$ s
Processing	
Bin size	12.5 m
Mean fold	100
Mute of NMO-distorted signals: maximum stretch	50%

from 17–19 June 2012 (Figure 6). The seismic acquisition parameters are listed in Table 2. Seismic data processing included 150–800 Hz band-pass filtering, NMO correction and stacking with 12.5 m binning. Processed seismic section #1, a 25 km long transect, is presented in Figure 9, with the associated CTD temperature profile acquired at the beginning of the line. The hydrological data demonstrates a marked seasonal thermocline, with a decrease in temperature of  $2.5^\circ\text{C}$  between 30 and 35 m. On the seismic data, a continuous high amplitude reflector clearly shows up at about 30 m. It correlates with the significant temperature contrast recognized as the thermocline on the CTD profile, and is therefore interpreted as its signature. The thermocline reflector is well defined and numerous vertical displacements induced by the internal waves can be recognized (Figure 9). The section therefore provides a detailed and continuous picture of the shallow structure of the ocean at a high lateral resolution of 12.5 m.

[68] The data set collected during the ASPEX cruise is probably too limited in size to allow an in-depth study of

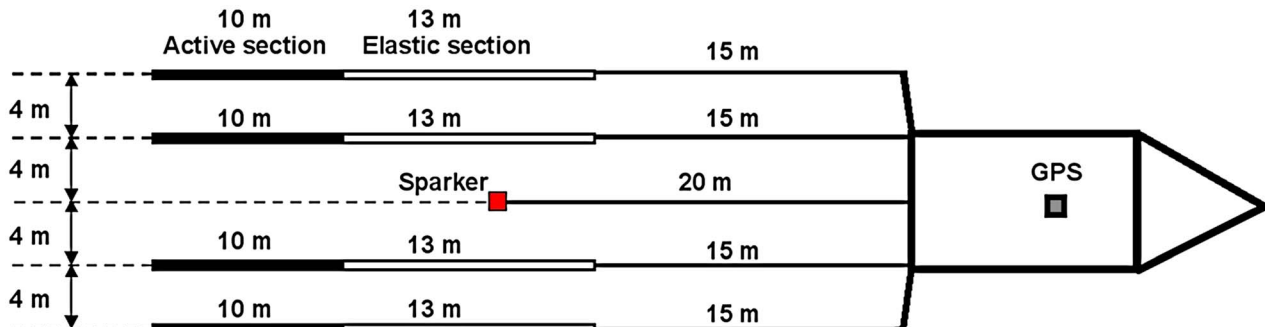


**Figure 8.** Geometry of the ASPEX seismic acquisition system.

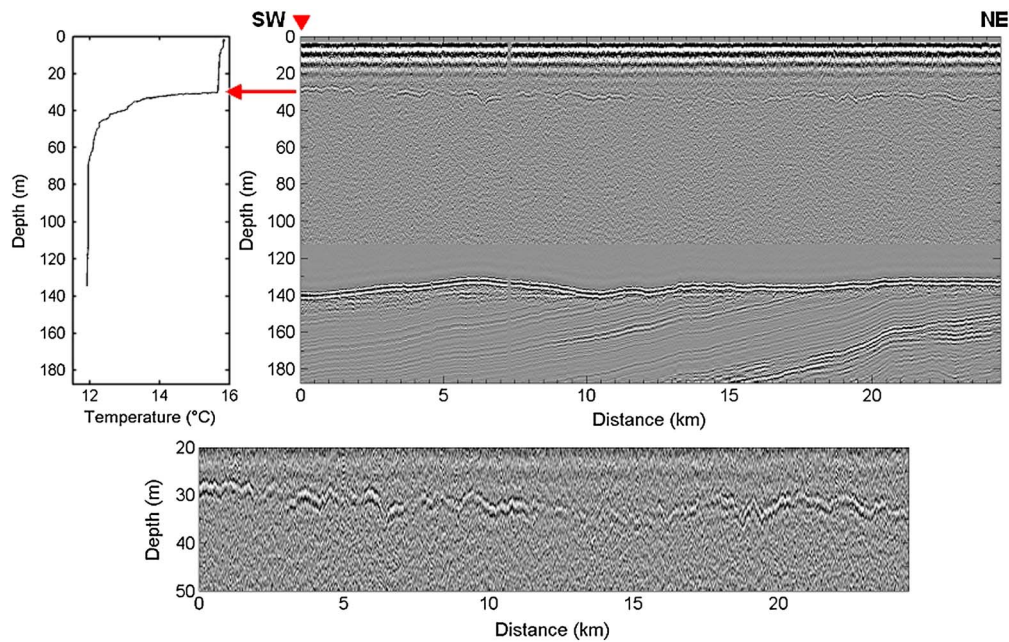


**Figure 9.** (top right) ASPEX processed seismic section #1. The red triangle denotes the position of the associated CTD station. The horizontal limit near 110 m corresponds to the depth below which an attenuation factor was applied to the amplitudes. The 30 m deep marked reflector is the signature of the thermocline. (top left) CTD temperature data acquired at the beginning of the seismic section. (bottom) Enlarged view of the thermocline reflector from the seismic section above. Vertical displacements of reflectors are most likely the result of internal wave motions.

internal wave field properties. However, several qualitative conclusions can be drawn:

[69] 1. The vertical displacements, although well resolved by the technique, are rather weak compared to the displacements observed at the end of summer in the Celtic Sea, to the north of the section [Pingree and Mardell, 1985]. This is not unexpected, as the survey was performed shortly after neap tides, at a period when the seasonal stratification was not fully established. Baroclinic tides produced at the shelf-break could thus be expected to be weaker, and to propagate less easily to the survey area [Pingree and New, 1995].

[70] 2. The phase velocity of mode 1 internal waves derived from the CTD profile is quite low, on the order of 10 cm/s. This translates to a semi-diurnal internal tide wavelength of roughly 5 km. Although much structure at the kilometric and subkilometric length scales is clearly apparent in the section, it is hard to see a significant periodic component at this or any longer wavelength. It thus remains unclear whether these small-scale structures are tidally forced, or if they correspond to a background internal waves field, of the family of spectral types described by Garrett and Munk [1972].

[71] 3. A slow dip of the thermocline, which is probably associated with the large-scale structure of the Armorican shelf “Bourrelet Froid” [Puillat et al., 2004], is also visible.

[72] Of these different structures, it is clear that only the large-scale dip is within reach of current state-of-the-art in situ measurement techniques. Using a towed undulating CTD package, the solution which currently provides the highest horizontal resolution, two successive crossings of the thermocline can be separated by several hundred meters

at best. This resolution severely aliases the subkilometric features of the thermocline, which appear as a strong noise component on the large-scale pattern. The data collected during the ASPEX cruise thus provide clear evidence of the importance of SO to the study of shallow submesoscale oceanographic structures.

## 6. Conclusion

[73] In this paper, it was demonstrated that successful high lateral resolution seismic imaging of the shallowest levels of the ocean can be achieved using a small- offset, multiple-streamer system and a high-resolution source, providing that (i) the source energy release is well-suited to the acoustic features of the environment, and its vertical resolution and signature length are relevant respectively to the scale and depth of the targeted structures; (ii) precise guidelines regarding the antenna filter issue and the multiple coverage are respected for the design of the receiver system; (iii) dedicated processing including data summing is applied. Using a short four-streamer array and a 1000J sparker, a detailed image of the 30 m deep seasonal thermocline on the western Brittany continental shelf was obtained, with what are most likely internal wave induced vertical displacements mapped at a 12.5 m lateral resolution. These results indicate that the seismic reflection technique can provide rapid, remote sensing images of small-scale horizontal variations of the shallow thermohaline structure of the ocean, at resolutions finer by two orders of magnitude than those achievable using state-of-the-art in situ techniques. Future work should further investigate these techniques in order to set up seismic tools

suitable for quantitative studies of such structures including the inversion of seismic data for temperature and salinity.

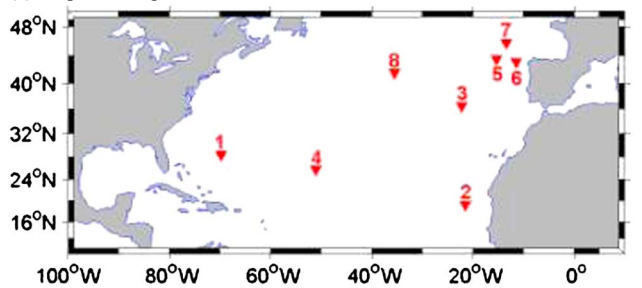
## Appendix A

**Table A1.** ARGO Floats and Map Showing Location of Floats

(a) ARGO Floats Analyzed in Section 2.1

Float number	Cycle	Date	Latitude	Longitude	Number on the Map
4901222	24	15 Aug 2011	28.370°N	69.777°W	1
6900695	100	24 Aug 2011	19.288°N	21.497°W	2
6900958	8	05 Sep 2011	36.472°N	22.162°W	3
6901053	5	15 Jul 2011	25.699°N	51.054°W	4
6900493	118	13 Sep 2011	43.521°N	15.308°W	5
6900763	69	23 Jul 2012	43.182°N	11.401°W	6
6900864	10	17 Jul 2011	45.742°N	13.351°W	7
6900582	25	08 Aug 2011	41.577°N	35.462°W	8

(b) Map Showing the Location of the Floats



[74] **Acknowledgments.** The authors wish to thank all the people who shared and provided data: R.W. Hobbs and L. Géli for the GO data, T. Mulder for the Carambar data, and Total-Exxon-Mobil and G. Jouet for the Sigolo data. We would also like to acknowledge the ARGO international program for providing public access to float data, in particular through the CORIOLIS database. Special thanks go to the crews of R/V Gwen Drez and R/V Côtes de la Manche, and to N. Mordant. Finally, the authors would like to thank Grant George Buffett, Berta Biescas Goriz and R.W. Hobbs for their helpful comments that greatly contributed to the improvement of this manuscript. This paper is part of the PhD work of H.P., which was funded by a stipend from the Région Bretagne.

## References

Biescas, B., L. Armi, V. Sallarès, and E. Gràcia (2010), Seismic imaging of staircase layers below the Mediterranean Undercurrent, *Deep-Sea Res. Pt. I*, *57*, 1345–1353, doi:10.1016/j.dsr.2010.07.001.

Biescas, B., V. Sallarès, J. L. Pelegrí, F. Machín, R. Carbonell, G. Buffett, J. J. Dañobeitia, and A. Calahorrano (2008), Imaging meddy finestructure using multichannel seismic reflection data, *Geophys. Res. Lett.*, *35*, L11609.

Blacic, T. M., and W. S. Holbrook (2010), First images and orientation of fine structure from a 3-D seismic oceanography data set, *Ocean Sci.*, *6*(2), 431–439.

Calvès, G., et al. (2012), Inferring denudation variations from the sediment record: An example of the last glacial cycle record of the Golo basin and watershed, *East Corsica, western Mediterranean Sea*, *Basin Res.*, *24*, 1–22, doi: 10.1111/j.1365-2117.2012.00556.x.

Carniel, S., A. Bergamasco, J. W. Book, R. W. Hobbs, M. Scavo, and W. T. Wood (2012), Tracking bottom waters in the Southern Adriatic Sea applying seismic oceanography techniques, *Cont. Shelf Res.*, *44*, 30–38, doi:10.1016/j.csr.2011.09.004.

Chapman, N. R., and A. Price (2011), Low frequency deep ocean ambient noise trend in the Northeast Pacific Ocean, *J. Acoust. Soc. Am.*, *129*, 161–165, doi: 10.1121/1.3567084.

Chapman, N. R., and J. W. Cornish (1993), Wind dependence of deep ocean ambient noise at low frequencies, *J. Acoust. Soc. Am.*, *93*, 782–789.

D’Ortenzio, F., D. Iudicone, C. De Boyer Montégut, P. Testor, D. Antoine, S. Marullo, R. Santoleri, and G. Madec (2005), Seasonal variability of the

mixed layer depth in the Mediterranean Sea as derived from in situ profiles, *Geophys. Res. Lett.*, *32*, L12605.

De Boyer Montégut, C., G. Madec, A. S. Fischer, A. Lazar, and D. Iudicone (2004), Mixed layer depth over the global ocean: An examination of profile data and a profile-based climatology, *J. Geophys. Res.*, *109*, C12003.

Fer, I., P. Nandi, W. S. Holbrook, R. W. Schmitt, and P. Páramo (2010), Seismic imaging of a thermohaline staircase in the western tropical North Atlantic, *Ocean Sci.*, *6*, 621–631.

Fortin, W. F. J., and W. S. Holbrook (2009), Sound speed requirements for optimal imaging of seismic oceanography data, *Geophys. Res. Lett.*, *36*, L00D01.

Garrett, C. J., and W. Munk (1972), Space-time scales of internal waves. *Geophys. Fluid Dyn.*, *2*, 255–264.

Géli, L., E. Cosquer, R. W. Hobbs, D. Klaeschen, C. Papenberg, Y. Thomas, C. Menesguen, and B. L. Hua (2009), High resolution seismic imaging of the ocean structure using a small volume airgun source array in the Gulf of Cadiz, *Geophys. Res. Lett.*, *36*, L00D09.

Géli, L., B. Savoye, X. Carton, and M. Stéphan (2005), Seismic imaging of the ocean internal structure: A new tool in physical oceanography?, *Eos, Trans. Amer. Geophys. Union*, *86*.

Hickey, B. M., P. MacCready, E. Elliott, and N. B. Kachel (2000), Dense saline plumes in Exuma Sound, Bahamas, *J. Geophys. Res.—Oceans*, *105*, 11471–11488.

Hobbs, R. W., D. Klaeschen, V. Sallarès, E. Vsemirnova, and C. Papenberg (2009), Effect of seismic source bandwidth on reflection sections to image water structure, *Geophys. Res. Lett.*, *36*, L00D08.

Holbrook, W. S., I. Fer, and R. W. Schmitt (2009), Images of internal tides near the Norwegian continental slope, *Geophys. Res. Lett.*, *36*, L00D10.

Holbrook, W. S., and I. Fer (2005), Ocean internal wave spectra inferred from seismic reflection transects, *Geophys. Res. Lett.*, *32*, L15604.

Holbrook, W. S., P. Páramo, S. Pearce, and R. W. Schmitt (2003), Thermohaline fine structure in an oceanographic front from seismic reflection profiling, *Science*, *301*, 821.

Jouet, G., S. Charrier, C. Labaune, G. Lericolais, E. Thereau, and Y. Thomas (2011), SiGolo program: Advanced processing (HR multi-channel Sparker seismic and multi-beam bathymetric data). Report of the Golo Program Phase 1: Brest, Ifremer—Total.

Jurado, E., H. J. van der Woerd, and H. A. Dijkstra (2012), Microstructure measurements along a quasi-meridional transect in the northeastern Atlantic Ocean, *J. Geophys. Res.—Oceans*, *117*.

Klein, P., and G. Lapeyre (2009), The oceanic vertical pump induced by mesoscale and submesoscale turbulence, *Ann. Rev. Mar. Sci.*, *1*, 351–375, doi: 10.1146/annurev.marine.010908.163704.

Klymak, J. M., and J. N. Moum (2003), Internal solitary waves of elevation advancing on a shoaling shelf, *Geophys. Res. Lett.*, *30*(20), 2045.

Krahmann, G., P. Brandt, D. Klaeschen, and T. Reston (2008), Mid-depth internal wave energy off the Iberian Peninsula estimated from seismic reflection data, *J. Geophys. Res.*, *113*, C12016.

Krim, H., and M. Viberg (1996), Two decades of array signal processing research. The parametric approach, *IEEE Signal Proc. Mag.*, 67–94.

Le Boyer, A., G. Cambon, N. Daniault, S. Herbet, B. Le Cann, L. Marié, and P. Morin (2009), Observations of the Ushant tidal front in September 2007, *Cont. Shelf Res.*, *29*, 1026–1037, doi:10.1016/j.csr.2008.12.020.

Le Corre, P., and V. Mariette (1985), Le front thermique d’Ouessant en août et septembre 1982: campagne SATIR-DYNATLANT, Ifremer, Brest.

Leaman, K. D., P. S. Vertes, L. P. Atkinson, T. N. Lee, P. Hamilton, and E. Waddell (1995), Transport, potential vorticity, and current/temperature structure across the Northwest Providence and Santaren Channels and the Florida Current Off Cay Sal Bank, *J. Geophys. Res.*, *100*, 8561–8569.

Lurton, X. (2002), *An Introduction to Underwater Acoustics: Principles and Applications*, Springer, London.

Menesguen, C., B. L. Hua, X. Carton, F. Klingelhoefer, P. Schnürle, and C. Reichert (2012), Arms winding around a meddy seen in seismic reflection data close to the Morocco coastline, *Geophys. Res. Lett.*, *39*, L05604.

Merchant, N. D., M. J. Witt, P. Blondel, B. J. Godley, and G. H. Smith (2012), Assessing sound exposure from shipping in coastal waters using a single hydrophone and Automatic Identification System (AIS) data, *Mar. Pollut. Bull.*, *64*.

Millero, F. J., C. T. Chen, A. Bradshaw, and K. Schleicher (1980), A new high pressure equation of state for seawater, *Deep Sea Res.*, *27*, 255–264.

Mirshak, R., M. R. Nedimovic, B. J. W. Greenan, B. R. Ruddick, and K. E. Loudon (2010), Coincident reflection images of the Gulf Stream from seismic and hydrographic data, *Geophys. Res. Lett.*, *37*, L05602.

Monterey, G., and S. Levitus (1997), *Seasonal Variability of Mixed Layer Depth for the World Ocean*, NOAA, Silver Spring, Md.

Mulder, T., et al. (2012a), New insights into the morphology and sedimentary processes along the western slope of Great Bahama Bank, *Geology*, *40*, 603–606, doi: 10.1130/G32972.1.

Mulder, T., et al. (2012b), Canyon morphology on a modern carbonate slope of the Bahamas: Evidence of a regional tectonic tilting, *Geology*, *40*, 771–774, doi: 10.1130/G33327.1.

- Mulder, T., et al. (2011), Modèle de dépôt sur une rampe carbonatée. *L'exemple des Bahamas—Résultats préliminaires de la campagne Carambar, Géochronique*, 118, 6–8.
- Nakamura, Y., T. Noguchi, T. Tsuji, S. Itoh, H. Niino, and T. Matsuoka (2006), Simultaneous seismic reflection and physical oceanographic observations of oceanic fine structure in the Kuroshio extension front, *Geophys. Res. Lett.*, 33, L23605.
- Nandi, P., W. S. Holbrook, S. Pearse, P. Páramo, and R. W. Schmitt (2004), Seismic reflection imaging of water mass boundaries in the Norwegian Sea, *Geophys. Res. Lett.*, 31, L23311.
- Phillips, J. D., and D. F. Dean (1991), Multichannel acoustic reflection profiling of ocean watermass temperature/salinity interfaces, in *Ocean Variability and Acoustic Propagation*, edited by J. Potter and A. Wam-Varnas, 199–214, Kluwer Academic Publishers, Dordrecht.
- Pickard, G. L., and W. J. Emery (1990), *Descriptive Physical Oceanography. An Introduction*, Pergamon Press, Oxford.
- Pingree, R. D., and A. L. New (1995), Structure, seasonal development and sun-glint spatial coherence of the internal tide on the Celtic and Armorican shelves and in the Bay of Biscay, *Deep Sea Res.*, 42, 245–284.
- Pingree, R. D., and G. T. Mardell (1985), Solitary internal waves in the Celtic Sea, *Prog. Oceanogr.*, 14, 431–441.
- Puillat, I., P. Lazure, A. M. Jégou, L. Lampert, and P. I. Miller (2004), Hydrographical variability on the French continental shelf in the Bay of Biscay during the 1990s, *Cont. Shelf Res.*, 24, 1143–1163, doi:10.1016/j.csr.2004.02.008.
- Quentel, E., X. Carton, M. A. Gutscher, and R. Hobbs (2010), Detecting and characterizing mesoscale and submesoscale structures of Mediterranean water from joint seismic and hydrographic measurements in the Gulf of Cadiz, *Geophys. Res. Lett.*, 37, L06604.
- Reygondeau, G., and G. Beaugrand (2011), Water column stability and *Calanus finmarchicus*, *J. Plankton Res.*, 33, 119–136, doi:10.1093/plankt/fbq091.
- Ruddick, B., H. B. Song, C. Z. Dong, and L. Pinheiro (2009), Water column seismic images as maps of temperature gradient, *Oceanography*, 22, 192–205.
- SAIC (1992), Straits of Florida physical oceanography field study, final interpretive report. Volume II: Technical Report, U.S. Dept. of The Interior, Minerals Management Service, Gulf of Mexico OCS Regional Office, New Orleans, LA.
- Sallarès, V., B. Biescas, G. Buffett, R. Carbonell, J. J. Dañobeitia, and J. L. Pelegrí (2009), Relative contribution of temperature and salinity to ocean acoustic reflectivity, *Geophys. Res. Lett.*, 36, L00D06.
- Sheriff, R. E., and L. P. Geldart (1982), *Exploration Seismology, History, Theory and Data Acquisition*, Vol.1, Cambridge University Press, Cambridge.
- Small, R. J., S. Carniel, T. Campbell, J. Teixeira, and R. Allard (2012), The response of the Ligurian and Tyrrhenian Seas to a summer Mistral event: A coupled atmosphere-ocean approach, *Ocean Model.*, 48, 30–44, doi:10.1016/j.ocemod.2012.02.003.
- Stephan, Y., J. M. Boutonnier, and C. Pistre (2012), Bilan des activités anthropiques génératrices de bruit sous-marin et de leur récente évolution en France métropolitaine, SHOM, Brest.
- Telford, W. M., L. P. Geldart, and R. E. Sheriff (1990), *Applied Geophysics*, 2nd Edition, Cambridge University Press, Cambridge.
- Trevorrow, M. V. (1998), Observations of internal solitary waves near the Oregon coast with an inverted echo-sounder, *J. Geophys. Res.—Oceans*, v. 103, p. 7671–7680.
- Tsuji, T., T. Noguchi, H. Niino, T. Matsuoka, Y. Nakamura, H. Tokuyama, S.I. Kuramoto, and N. Bangs (2005), Two-dimensional mapping of fine structures in the Kuroshio Current using seismic reflection data, *Geophys. Res. Lett.*, v. 32, L14609.
- Vetrano, A., E. Napolitano, R. Iacono, K. Schroeder, and G. P. Gasparini (2010), Tyrrhenian Sea circulation and water mass fluxes in spring 2004. Observations and model results: *J. Geophys. Res.—Oceans*, v. 115.
- Warner, M., and S. McGeary (1987), Seismic reflection coefficients from mantle fault zones, *Geophys. J. Int.*, v. 89, p. 223–230.
- Wennekens, M. P. (1959), Water mass properties of the Straits of Florida and related waters, *B. Mar. Sci.*, v. 9, p. 1–52.
- Widess, M. B. (1973), How thin is a thin bed?, *Geophysics*, 38, p. 1176–1180.
- Yilmaz, O. (1987), *Seismic Data Processing*, Society of Exploration Geophysicists, Tulsa, Ok.
- Zoeppritz, K. (1919), Erdbebenwellen VII. VIIb. Über Reflexion und Durchgang seismischer Wellen durch Unstetigkeitsflächen, Nachrichten von der Königlichen Gesellschaft der Wissenschaften zu Göttingen, Mathematisch-physikalisch Klasse, p. 66–84.